

Small-angle Neutron Scattering Studies of Pore Filling in Carbon Electrodes: Mechanisms Limiting Lithium-Air Battery Capacity

Tatiana K. Zakharchenko,^{1,2} Mikhail V. Avdeev,² Artem V. Sergeev,^{3,1} Alexander V. Chertovich,¹ Oleksandr I. Ivankov,² Victor I. Petrenko,² Yang Shao-Horn,⁴ Lada V. Yashina,¹ Daniil M. Itkis^{1}*

¹Lomonosov Moscow State University, Leninskie gory 1/3, 119991 Moscow, Russia,

²Frank Laboratory of Neutron Physics Joint Institute for Nuclear Research, Joliot-Curie str. 6, Dubna, 141980 Moscow reg., Russia

³Skolkovo Institute of Science and Technology, Nobel str. 3, 121205 Moscow, Russia

⁴Materials Science and Engineering Department, Massachusetts Institute of Technology, 3-334, 77 Massachusetts Avenue, Cambridge, MA 02139, USA, Massachusetts 02139, United States

*E-mail: yashina@inorg.chem.msu.ru

Table of contents

Carbon paper properties	3
Calculation details	5
Additional discharge curves	6
Determination of appropriate electrolyte volume	7
Neutron data processing	8
Scattering curves for discharged electrodes	8
SLD calculation	9
Carbon paper SLD determination	10
Correction for the incoherent background	12
<i>Pristine electrodes</i>	12
<i>Electrodes upon discharge</i>	13
Volume fraction and specific surface area of open pores in pristine electrode material	14
Li₂O₂ diffraction peak approximation	15
References	16

Carbon paper properties

Table S1. SIGRACET #4412 Carbon paper properties

Parameter	Value
Thickness	380 μm
Areal weight	7.7 mg/cm^2
Surface area (BET)	18 m^2/g
Carbon black particles mean size	50 \pm 13 nm

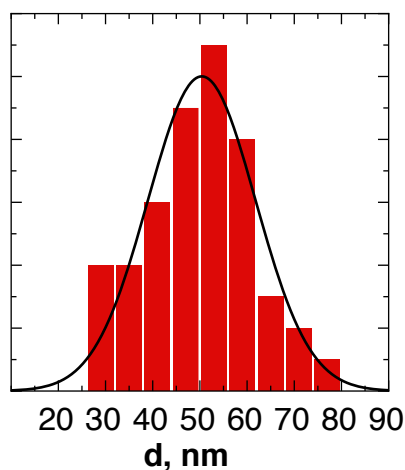


Figure S1. SIGRACET #4412 carbon black particles size distribution. The size distribution was estimated by a statistical analysis of SEM image with approximately 100 particles counted in total.

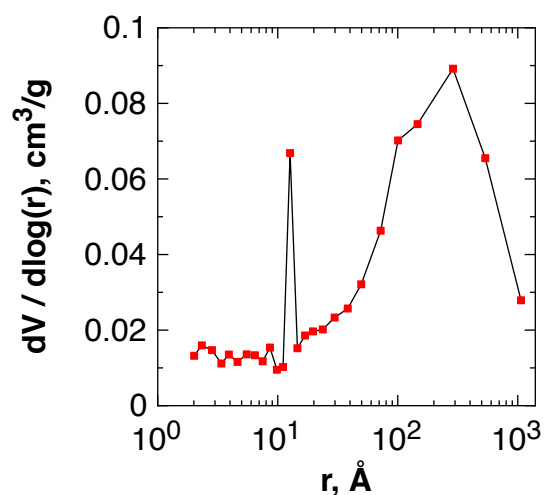


Figure S2. SIGRACET #4412 BJH pore size distribution

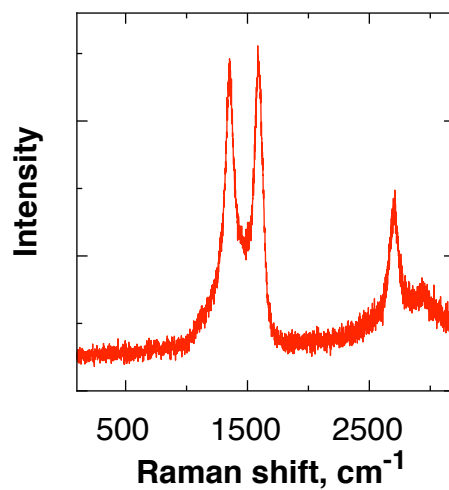


Figure S3. Raman spectra of SIGRACET #4412. Raman scattering spectra were collected with a Renishaw inVia microscope with Ar⁺-laser operating at 514 nm wavelength

Calculation details

Table S2. Parameters used in numerical simulations

Parameter	Value
Temperature, T	293 K
Open circuit cell voltage, $U_c - U_a$	2.96 V vs Li/Li ⁺ [1]
Initial electrolyte concentration, $c_{e,0}$	1 mol/L
Anode exchange current, i_{0a}	12.6 A/m ² [2]
Cathode reaction rate constant, k_0	$1 \cdot 10^{-8}$ m/s (assumed, see [3] for details)
Electrolyte conductivity, k	1 S/m [4]
Li ⁺ diffusion coefficient, D_+	$1.7 \cdot 10^{-10}$ m ² /s [4]
Anion diffusion coefficient, D_-	$4.9 \cdot 10^{-10}$ m ² /s [4]
Cation mobility, u_+	$2.8 \cdot 10^{-14}$ m/sN [4]
Oxygen diffusion coefficient, D_{O_2}	$4.64 \cdot 10^{-10}$ m ² /s [5]
Oxygen solubility (@ 1 atm.), $c_{O_2}^0$	6.0 mM
Carbon conductivity, σ	100 S/m
Discharge product resistivity, $R_{Li_2O_2}$	$5.0 \cdot 10^{-10}$ Ω m (fitted)
Carbon density, ρ_c	2.26 g/cm ³
Molar mass of Li ₂ O ₂ , $M_{Li_2O_2}$	45.88 g/mol
Gravimetric density of Li ₂ O ₂ , $\rho_{Li_2O_2}$	2.31 g/cm ³
Initial small pore radius, r_0	15 nm
Small pore volume fraction	3%
Solid phase (carbon) volume fraction	12%

Additional discharge curves

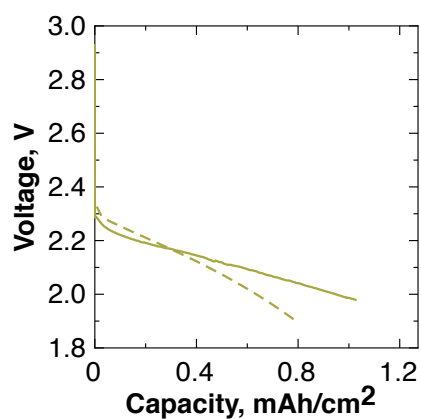


Figure S4. Experimental (solid) and simulated (dashed) galvanostatic Li-O₂ discharge curves for carbon paper electrodes in 1M LiTFSI in MeCN at 500 $\mu\text{A}/\text{cm}^2$.

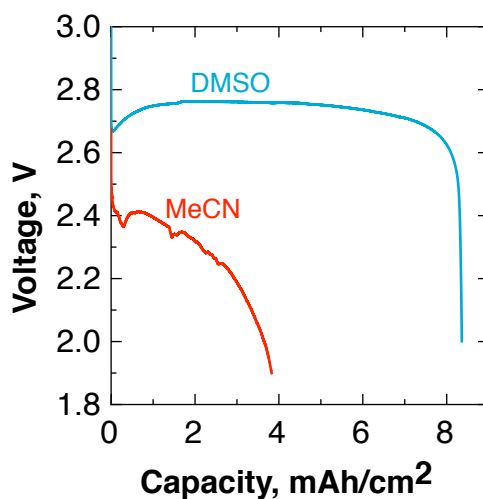


Figure S5. Galvanostatic Li-O₂ discharge curves for carbon paper electrodes in 1M LiTFSI in MeCN and 1M LiTFSI in DMSO at 100 $\mu\text{A}/\text{cm}^2$ that have been used in SEM experiment.

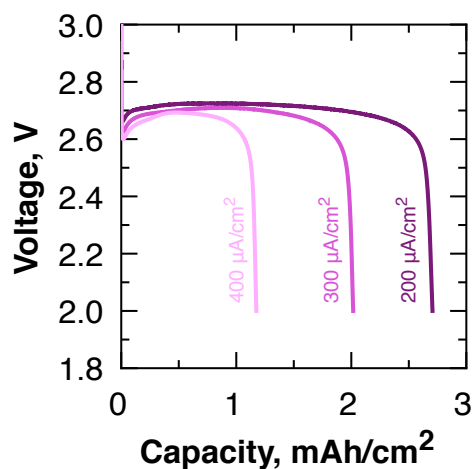


Figure S6. Galvanostatic Li-O₂ discharge curves of carbon paper electrodes in 1M LiTFSI in DMSO with 150 ppm of water at various current densities.

Determination of appropriate electrolyte volume

For determination of appropriate electrolyte volume for utilization of whole volume of accessible pores we measured CVs of the cell with various electrolyte volume. Results are shown in Fig. S7. Here, we can see that EDL charging current increases together with electrolyte volume. For subsequent experiments with DMSO-based solvent 130 μl was chosen as an appropriate volume. For experiments with MeCN 300 μl was added to each cell since MeCN is highly volatile solvent.

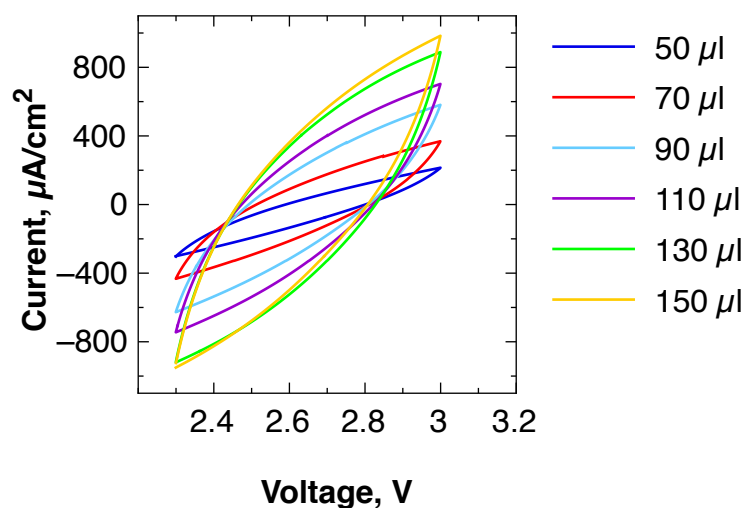


Figure S7. CV for carbon paper electrodes in 1M LiTFSI DMSO in Ar with various electrolyte volume.

Neutron data processing

Scattering curves for discharged electrodes

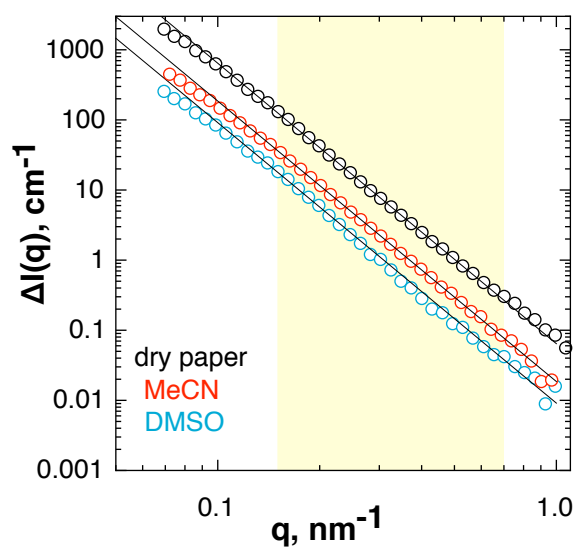


Figure S8. Fragment of differential SANS curves at low q values for dry electrode and electrodes, which were galvanostatically discharged in 1 M LiTFSI in DMSO and MeCN at $200 \mu\text{A}^2\text{cm}^{-2}_{\text{geom}}$. Solid lines shows Porod approximation. Region of Porod approximation (0.15 - 0.7 nm^{-1}) is colored in yellow.

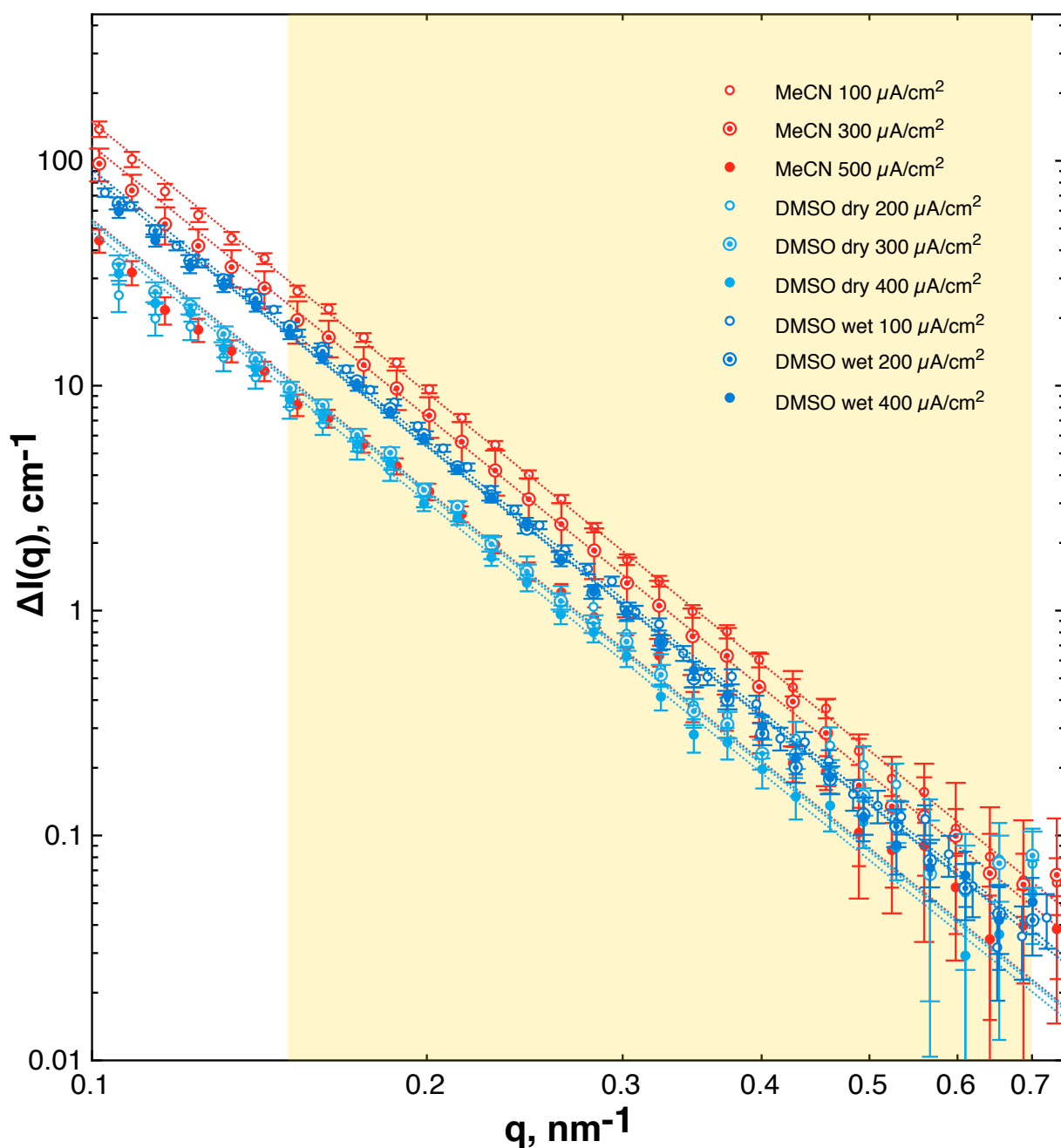


Figure S9. Fragment of differential SANS curves at low q values for galvanostatically discharged electrodes in 1 M LiTFSI in MeCN and DMSO.

SLD calculation

SLDs were calculated using the common software available online [6].

Table S3. Properties of the cell components and the calculated SLD values.

	Chemical formula	M, g mol⁻¹	ρ, g cm⁻³	SLD, $\times 10^{10}$ cm⁻²
Carbon black	C	12.01	2.15	7.17
Lithium peroxide	Li ₂ O ₂	45.88	2.31	2.37
LiTFSI	LiN(CF ₃ SO ₂) ₂	287.09	1.33	2.34
DMSO	(CH ₃) ₂ SO	78.13	1.10	-0.004
DMSO-d ⁶	(CD ₃) ₂ SO	84.17	1.19	5.28
Acetonitrile	CH ₃ CN	41.05	0.79	1.32
Acetonitrile-d ³	CD ₃ CN	44.07	0.84	4.92

1M LiTFSI

1 M Li TFSI /d⁶-DMSO:

$$\phi = 1 \times 10^{-3} \text{ mol/cm}^3$$

$$m / \rho = 1 \times 10^{-3} \times 287.09 / 1.334 = 0.2152;$$

$$\text{SLD} = 0.2152 \times 2.3392 + (1 - 0.2152) \times 5.2781 = 4.64565 \times 10^{10} \text{ cm}^{-2}$$

1 M Li TFSI /d³-MeCN:

$$\phi = 1 \times 10^{-3} \text{ mol/cm}^3$$

$$m / \rho = 1 \times 10^{-3} \times 287.09 / 1.334 = 0.2152;$$

$$\text{SLD} = 0.2152 \times 2.3392 + (1 - 0.2152) \times 4.9222 = 4.1493 \times 10^{10} \text{ cm}^{-2}$$

Carbon paper SLD determination

To separate the contributions from open and closed pores, and analyze their changes with the contrast variation, first, the curve from pristine soaked electrode and the difference curve between pristine dry and pristine soaked electrodes are considered in Fig. S10, where all the curves are corrected for the incoherent background (the details are given below). As one can see, at sufficiently large q -values the two curves are of the power-law type with significantly different exponents. Fig. S10 clearly shows that the transformation of the initial curve from the pristine dry electrode to the curve from the soaked electrode is mainly related to the variation in the level ‘open pores’; the scattering for the level ‘closed pores’ at large q -values remains unchanged. The fact that the exponent in the power-law scattering in the difference curve satisfies the Porod law, $I(q) \sim q^{-4}$, is a strong indication that this curve represents mainly the scattering from the open pores, which are further filled with the solvent and matched at some extent against the carbon paper. It is important that this procedure does not change the q -dependence, and only the absolute intensity varies following the changes in the squared contrast factor

$$(\Delta\rho)^2 = (\rho_s - \rho)^2 \quad (\text{S1})$$

which is the squared difference between SLDs of the carbon-based matrix of the paper, ρ_s , and the pores, ρ . Since in the dry state the pores are empty, then $\rho = 0$, and $(\Delta\rho)^2 = (\rho_s)^2$. After the pores are filled, the scattering from them is proportional to $(\rho_s - \rho_e)^2$, where ρ_e is SLD of electrolyte, i.e. the absolute intensity at the level ‘open pores’ is reduced by the factor of $\varepsilon^2 = (\rho_s - \rho_e)^2 / (\rho_s)^2$. Let us denote the experimental curves from pristine dry and soaked electrodes as $I_1(q)$ and $I_2(q)$, respectively, and introduce the scattering from the open pores at $\rho = 0$, $I_{op}(q)$, and the scattering from the closed pores, $I_{cl}(q)$, which is insensitive to the contrast. Then, one can write:

$$I_1(q) = I_{op}(q) + I_{cl}(q) \quad (\text{S2a})$$

$$I_2(q) = \varepsilon^2 I_{op}(q) + I_{cl}(q) \quad (\text{S2b})$$

The simplest calculations give:

$$I_{op}(q) = \frac{I_1(q) - I_2(q)}{1 - \varepsilon^2} \quad (S3)$$

To evaluate further the contrast reduction factor ε^2 and, hence, determine ρ_s , we used analysis of the curves for the two levels, which was based on the universal exponential/power-law approximation combining the Guinier regime at small q -values with the power-law type scattering at large q -values [7]. For the difference curve it gives:

$$I_1(q) - I_2(q) = G e^{-\frac{q^2 R^2}{3}} + B \left(\frac{1}{q^*}\right)^P \quad (S4)$$

where

$$q^* = \frac{q}{\left(\operatorname{erf}\left(\frac{qkR}{\sqrt{6}}\right)\right)^3} \quad (S4a)$$

and k is an empirical constant equal to 1 or 1.1 for the volume- or surface-type scattering, respectively, depending on the interval where the P exponent is varied (here, $k = 1.1$). For the difference curve in Fig. S10 one obtains $G = 7000 \pm 900 \text{ cm}^{-1}$, $R = 31.3 \pm 1.4 \text{ nm}$, $B = (6.3 \pm 0.3) \times 10^{-5}$, $P = 4.00 \pm 0.01$. As the next step, in accordance with (S2) and (S3) the curve from the soaked electrode was modeled as a sum of two contributions of type (S4):

$$\begin{aligned} I_2(q) &= \varepsilon^2 I_{op}(q) + I_{cl}(q) = \frac{\varepsilon^2}{1 - \varepsilon^2} (I_1(q) - I_2(q)) + I_{cl}(q) = \\ &= \frac{\varepsilon^2}{1 - \varepsilon^2} \left(G e^{-\frac{q^2 R^2}{3}} + B \left(\frac{1}{q^*}\right)^P \right) + \left(1 - \frac{\varepsilon^2}{1 - \varepsilon^2} \right) \left(G_{cl} e^{-\frac{q^2 R_{cl}^2}{3}} + B \left(\frac{1}{q_{cl}^*}\right)^{P_{cl}} \right) \end{aligned} \quad (S5).$$

Parameters in (S5) denoted by index ‘cl’ are referred to the intensity $I_{cl}(q)$. Here, we used the fact that, as compared to (S4), the scattering from the open pores is reduced by the factor $\frac{\varepsilon^2}{1 - \varepsilon^2}$. Parameters of (S4) were fixed at the values found above. Also, for $I_{cl}(q)$ the parameters of the power-law term were taken from the independent fit of $I_2(q)$ at large q -values, $B_{cl} = (1.16 \pm 0.02) \times 10^{-2}$, $P_{cl} = 2.34 \pm 0.01$, and fixed. Finally, the experimental curve $I_2(q)$ was fitted to Eq.S5 by varying just three parameters including ε , G_{cl} and R_{cl} , which gave $\varepsilon = 0.06 \pm 0.02$, $G_{cl} = 240 \pm 30 \text{ cm}^{-1}$, and $R_{cl} = 27.7 \pm 1.3 \text{ nm}$. The corresponding contrast reduction factor, $\varepsilon^2 \sim 0.004$. The calculated contribution from the open pores corresponding to this reduction factor is shown in Fig. S10 for comparison with $I_2(q)$.

$$\text{It gives } \rho_s = \frac{\rho_e}{1 - \varepsilon} = 4.943 \times 10^{10} \text{ cm}^{-2}.$$

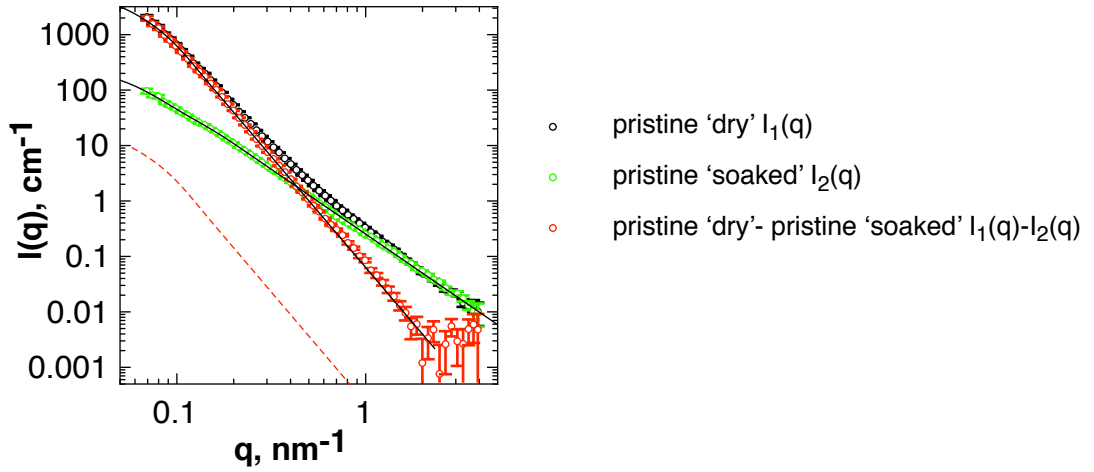


Figure S10. Model exponential/power-law approximations (solid lines) to the scattering at two levels corrected for background. The exponents in the characteristic power-law dependences for the two curves are indicated. Dashed line shows the calculated scattering contribution to $I_2(q)$ by the reduced scattering the open pores filled with the electrolyte.

Correction for the incoherent background

Pristine electrodes

To correct the experimental SANS curves from the pristine electrode for the incoherent background we used the clearly observed asymptotic behavior of the power-law type:

$$I(q) = \frac{B}{q^p} + C \quad (\text{S6})$$

First, the experimental curve from pristine ‘soaked’ electrode, which shows this behavior at sufficiently large q -values (see Fig. S11), was fitted to Eq. S6. Then, the curve corrected for the background was subtracted from the experimental scattering curve by ‘dry’ electrode. The resulting curve shows a distinct power-law dependence at large q -values (see Fig. S11) and was also fitted to Eq. S6. The resulting model curves are given in Fig. S11 together with the obtained power-law exponents. The found background values for the two curves are 0.009 ± 0.001 and $-0.001 \pm 0.0007 \text{ cm}^{-1}$, respectively. The negative value in the second case means that the background scattering in the preliminary treatment (scattering from the empty sample cell as described in the ‘Experimental’ section) was overestimated. These found values were used to obtain the scattering curves in Fig. S10

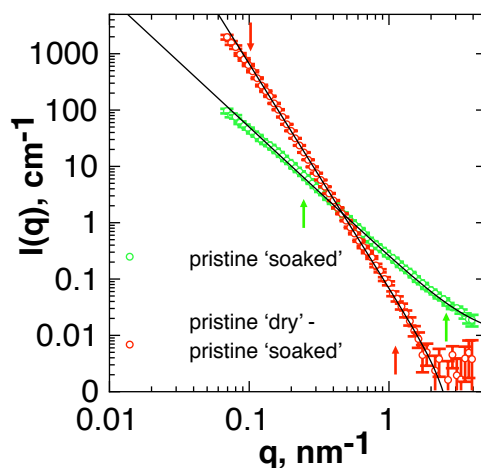


Figure S11. Fits of experimental SANS curves (points) to Eq. S6. Arrows show the intervals used in the fits. Solid lines are the best model curves. The corresponding specific power-law dependences are denoted.

Electrodes upon discharge

The correction of the experimental SANS curves from the electrodes upon discharge was made basing on the comparison with the scattering curve from the pristine ‘soaked’ electrode, $I_2(q)$. The procedure is illustrated in Fig. S12 for one of the fully discharged samples. In Fig. S12a one can see a difference in the incoherent background at largest q -values. The additional side effect, which is strongly stochastic for all samples, is a slight difference between the curves in the q -region below $q \sim 1 \text{ nm}^{-1}$. Here, the curves differ by some factor, which is related to the deviations ($\pm 10\%$) in the sample thickness (in the calibration procedure the thickness of $400 \mu\text{m}$ was set for all samples in accordance with the properties of the used electrode paper). In Fig. S12a the regions of the corrections are denoted by the dashed ovals. To correct the curves, the ratio $I(q)/I_2(q)$ was plotted (see Fig. S12b). Then, the subtracted background value and the coefficient regulating the absolute intensity of the curve under correction were simultaneously varied to fit the considered ratio to unity in the denoted region. This procedure assumes that the curves with the almost matched open pores should repeat the $I_2(q)$ curve at large q -values (scattering from closed pores) besides the interval where the diffraction peak appears during the discharge. The resulting ratio between the corrected in this way curve and $I_2(q)$ is also shown in Fig. S12b, while the curve itself is plotted in Fig. S12c, again in comparison with $I_2(q)$. The $I_2(q)$ curve was then subtracted from the corrected curves for the electrodes under discharge. The corresponding difference curves are shown in the main text in Fig. 4a,b.

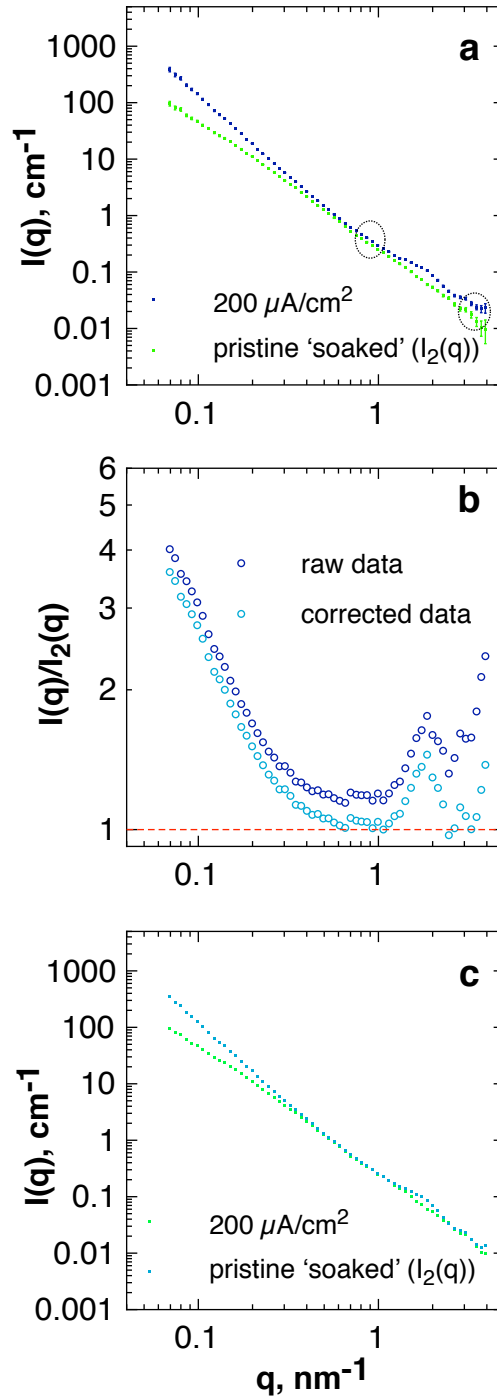


Figure S12. Steps of the correction of the scattering curves from electrodes under discharge for the incoherent background and electrode thickness. In (a) the regions of the corrections are denoted by the dashed ovals. Example is given for the fully discharged electrode under the current density of $200 \mu\text{A cm}^{-2}$.

Volume fraction and specific surface area of open pores in pristine electrode material

The volume fraction of the open pores at the scale below 100 nm was estimated using the Porod invariant:

$$Q = \int q^2 I(q) dq \quad (\text{S7})$$

The approximation to $I_{op}(q)$ according to Eq. S4 was used to increase the q -range and, hence, the precision in Q . The corresponding dependence $q^2 I_{op}(q)$ used is given in Fig. S13a. The obtained Q -invariant, $1.2 \times 10^{21} \text{ cm}^{-4}$, was related to the volume fraction of the open pores, φ , by the standard equation:

$$Q = 2\pi^2(\Delta\rho)^2\varphi(1 - \varphi) \quad (\text{S8})$$

where $(\Delta\rho)^2 = (\rho_s)^2$, ρ_s is the matrix SLD, and from the estimated $\rho_s = 4.943 \times 10^{10} \text{ cm}^{-2}$. Then, Eq. S8 gives $\varphi \sim 0.026$.

The specific area, S/V , of the open pores was also estimated from the Porod asymptotic behavior of $I_{op}(q)$ at large q -values:

$$\lim_{q \rightarrow \infty} (q^4 I(q)) = 2\pi(\Delta\rho)^2 \frac{S}{V} \approx B \quad (\text{S9})$$

where B is the parameter from the power-law type approximation (S4). The corresponding dependence $q^4 I_{op}(q)$ is demonstrated in Fig. S13b. From $B = 6.295 \times 10^{28} \text{ cm}^{-5}$ known from the fit and the contrast $\Delta\rho_s$ one obtains $S/V \sim 4.1 \text{ m}^2 \text{ cm}^{-3}$.

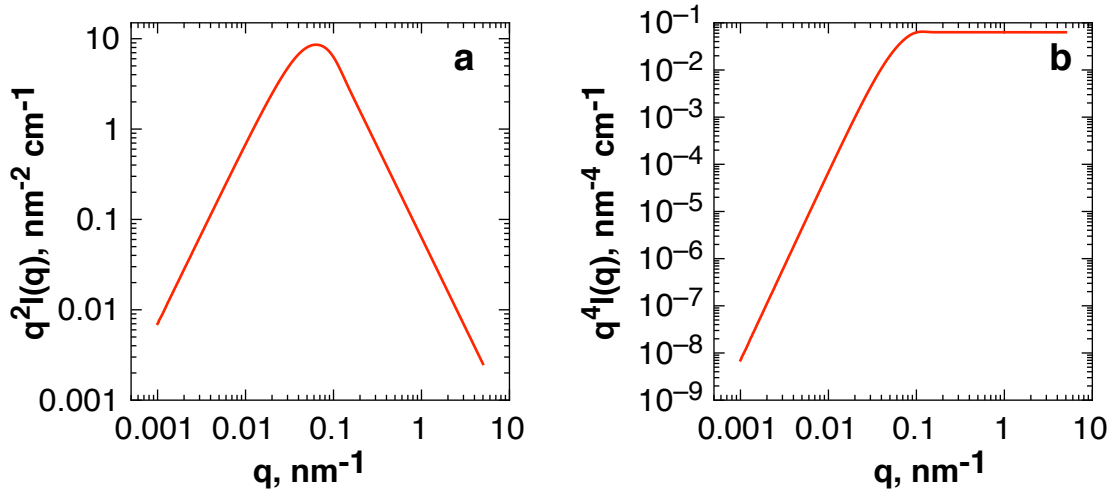


Figure S13. (a) The dependence $q^2 I_{op}(q)$ used in the integration Eq. S7 for the Q -invariant. (b) The dependence $q^4 I_{op}(q)$ illustrating the Porod limit Eq. S9.

Li₂O₂ diffraction peak approximation.

The curves are modeled in Fig.6c using the Eq. S10 combining power-law and the scattering describing the diffraction peak in a Gaussian approximation:

$$I_n(q) - I_2(q) = B \left(\frac{1}{q^*} \right)^P + A e^{-\frac{(q-q_0)^2}{2w^2}} + C \quad (\text{S10})$$

Modeled parameters are listed in table S4.

Table S4. Fitting parameters for high-q value region for scattering

Parameter	Value
B	0.0118(3) cm ⁻¹
R	37.9(5) nm
P	-3.85(1)
A	0.020(1) cm ⁻¹
q ₀	1.88(2) nm
w	0.25(2) nm
C	0.0012(4) cm ⁻¹

References

- [1] I. Kowalczyk, J. Read, M. Salomon, Li-air batteries: A classic example of limitations owing to solubilities, *Pure Appl. Chem.* 79 (2007) 851–860. doi:10.1351/pac200779050851.
- [2] M. Doyle, T.F. Fuller, J. Newman, Modeling of Galvanostatic Charge and Discharge of the Lithium/Polymer/Insertion Cell, *J. Electrochem. Soc.* 140 (1993) 1526–1533. doi:10.1149/1.2221597.
- [3] A.V. Sergeev, A.V. Chertovich, D.M. Itkis, E.A. Goodilin, A.R. Khokhlov, Effects of cathode and electrolyte properties on lithium–air battery performance: Computational study, *J. Power Sources.* 279 (2015) 707–712. doi:10.1016/j.jpowsour.2015.01.024.
- [4] A. Nyman, M. Behm, G. Lindbergh, Electrochemical characterisation and modelling of the mass transport phenomena in LiPF₆–EC–EMC electrolyte, *Electrochimica Acta.* 53 (2008) 6356–6365. doi:10.1016/j.electacta.2008.04.023.
- [5] C.O. Laoire, S. Mukerjee, K.M. Abraham, E.J. Plichta, M.A. Hendrickson, Influence of Nonaqueous Solvents on the Electrochemistry of Oxygen in the Rechargeable Lithium–Air Battery, *J. Phys. Chem. C.* 114 (2010) 9178–9186. doi:10.1021/jp102019y.
- [6] SLD Calculator <https://sld-calculator.appspot.com> (accessed 17 September 2018)
- [7] G. Beaucage, Small-Angle Scattering from Polymeric Mass Fractals of Arbitrary Mass-Fractal Dimension, *J Appl Crystallogr.* 29 (1996) 134–146. doi:10.1107/S0021889895011605.